Exchange bias in graphene multilayers/Co composites

Hua-Shu Hsu[1*], Yu-Ying Chang[1], Yi-Ying Chin[2*], Hong-Ji Lin[2], Chien-Te Chen[2], Shih-Jye Sun[3*], Sergey Zharkov[4,5], Chun-Rong Lin[1]& Sergey G. Ovchinnikov[4,5]

[1]Department of Applied Physics, National Pingtung University, Pingtung 900, Taiwan, R. O. C.

[2]National Synchrotron Radiation Research Center, Hsinchu 300, Taiwan, R. O. C.

[3]Department of Applied Physics, National University of Kaohsiung, Kaohsiung 811, Taiwan, R. O. C.

[4]Siberian Federal University, Krasnoyarsk, 660041, Russia

[5]L.V. Kirensky Institute of Physics, SB RAS, Krasnoyarsk, 660036, Russia

*hshsu@mail.nptu.edu.tw, chin.yiying@nsrrc.org.tw, sjs@nuk.edu.tw

Abstract

The exchange bias (EB) effect, which is the shift of the hysteresis loop of a ferromagnet in direct contact with an antiferromagnet, is highly advantageous for the development of spintronics applications. Carbon (C) has been considered as a potential material in next generation electronics production as well as spintronics devices beyond silicon. However, the EB effect has never been reported in C structures. Here we show experimental evidence for an EB in C/Co composites. We apply suitable annealing to induce graphitization by metal contact and thus induce EB at the interfacial antiferromagnetic coupling between Co and local graphene multilayers in a C matrix. The present work makes an advance in this field, as it reports an unexpected EB effect of a C based material.

When materials with ferromagnetic (FM) and antiferromagnetic (AFM) interfaces are cooled through the Neel temperature (T_N) of the AFM layer (with the Curie temperature, T_C, of the FM larger than T_N) an anisotropy is induced in the FM[1-3]. The magnetization of an FM layer is pinned into a well-defined reference direction by an AFM such that its hysteresis loop exhibits a horizontal shift. The field shift of the magnetic hysteresis loop, which is called exchange bias (EB), is from unpinned FM spins having their field response inhibited from coupling to pinned AF spins; essentially AF domains provide a field-dependent torque on the FM film's domains. The EB effect has become an integral part of spintronics, with implications for basic research and with numerous applications to devices, such as random access magnetic storage units and spin valves[4-5]. Carbon (C) has been considered as a potential material for next generation electronics production as well as for spintronics devices beyond silicon. Moreover, the interfacial effects between FM transitional metals (TMs) and C-based materials have attracted considerable attention. The magnetic proximity effects in transitional metal(TM)/carbon systems have also been evidenced by x-ray magnetic circular dichroism (XMCD)[6-8], ultraviolet-visible (UV-VIS) magnetic circular dichroism MCD[9,10], and polarized neutron reflectivity[8]. The origin of both the EB phenomenon and the magnetic proximity effect is an interlayer exchange coupling[11]. As a result, these two novel phenomena may occur simultaneously in a single system. However, sometimes one may be present, while the other remains absent; such situations motivate researchers to seek an EB effect in C/TM structures. However, this effect has never been reported in C/TM structures.

Amorphous carbon (*a*-C) is an amorphous semiconductor with a mixture of sp^2 and sp^3 hybridizations[12]. Large *a*-C films can be grown easily and they are compatible with various substrates. However, the modulation of the properties of *a*-C can be challenging. Practitioners understand that, with respect to the C microstructure, the presence of a metal promotes the formation of sp^2-bonded C nanostructures by metal-contact-induced graphitization following suitable annealing[13-17]. In this work, multilayer *a*-C/Co composites are fabricated using rapid thermal annealing (RTA) and the structures and magnetic properties of those composites are investigated. Magnetization and XMCD measurements reveal an EB at the interface between Co and graphene multilayers in the *a*-C matrix after RTA via antiferromagnetic (AFM) coupling. This is further supported by theoretical calculations. The present work makes an advance in this field, because it reports an unexpected EB effect in a C based material.

Results

The observation of EB in C/Co after RTA. Figure 1 shows the magnetic field dependent magnetization (M-H) data with applied fields along the in-plane axis for

a-C/Co composites without and with RTA at 10 K. An annealing temperature of 600°C was chosen to decompose the metastable Co–C bonds and form adequate *a*-C/Co interfaces. Figure 1 shows the M-H data with the applied field along the in-plane axis for (a) d = 3 nm and (b) d = 6 nm *a*-C/Co composites with and without RTA at 10 K. The hysteresis loops of these samples after RTA completely shifted to the left of the zero field axis, clearly indicating pronounced EB. The EB fields for d = 3 nm and d = 6 nm samples with RTA (given by the shift of the hysteresis loop along the H-axis) are HE 503 Oe and 291 Oe, respectively. By contrast, M-H data from the same samples without RTA exhibit no shift of the hysteresis loop. The $T^{1/2}$ dependence of Hc(T) (shown in the Fig. 1(c)) is a signature of thermal fluctuations dominating domain wall motion energetics and exchange coupling[18]. The blocking temperature, TB, (i.e., the temperature at which biasing vanishes) for these samples is about 200 K as shown in the Fig. 1(d). Further electronic- and micro-structures studies are necessary to clarify the phenomenological characteristics of this unexpected EB effect in *a*-C/C films after RTA.

Local structures, electronic structures, and microstructures of *a*-C/Co with and without RTA. Extended x-ray absorption fine structure (EXAFS) spectroscopy, a specialized version of X-ray absorption spectroscopy (XAS), was utilized to show the local structures that surrounded the Co atoms. Figure 2(a) plots the radial distribution function, the Fourier-transformed (FT) EXAFS amplitude of extended x-ray absorption fine structure (EXAFS), on the Co K-edge for these samples; it also plots the function on the Co-K edge of Co metal as a reference. A comparison with the peak associated with Co-Co bonding reveals that the spectra of the as-grown *a*-C/Co sample are dominated by peaks around 1.8 Å, probably associated with Co-C bonding[19,20]. It changes significantly after RTA. The Co *K*-edge FT spectra are very similar to spectra from Co metal. The results demonstrate that, in high vacuum RTA, most of the Co-C bonding decomposes and Co atoms form metallic clusters precipitated in the *a*-C matrix without forming a CoO phase. Because X-ray absorption near-edge structure (XANES) spectroscopy is a powerful tool for identifying electronic states, and particularly the valence states of TM elements, it was applied here. Figure 2(b) presents the XANES spectra on the Co K-edge of the d = 3 nm and d = 6 nm samples with and without RTA, together with that of a standard Co metal for comparison. Unlike the clear shoulder around 7712 eV in the Co metal spectra, the pre-edge features for d = 3 nm and d = 6 nm samples without RTA, which arise from the transition to bound states, reveal the appearance of Co-C bonds. In addition, both samples include a comparatively strong white line, which indicates a high concentration of unoccupied states. We believe that in these samples, the empty states of Co result from electrons that transfer from Co atoms onto C neighbors at the C/Co interfaces. Therefore, we suppose that the

origin of the enhanced XANES white line is caused by the appearance of a relatively high value of Co-C bonding. However, the Co-C bonding is metastable. After RTA, the carbide is decomposed, and therefore most of the Co atoms in d = 3 nm and d = 6 nm samples are close to the +0 metallic state. This result is consistent with our EXAFS data. However, it is noted that the difference near the white line of the XANES data between Co metal and RTA samples implies the empty states of Co result from the electron transfer from Co atoms onto graphitic neighbors at the C/Co interfaces. The d = 3 nm sample after RTA yields a spectrum that is between that of the d = 6 nm sample after RTA and that of metallic Co. The d = 6 nm sample after RTA reveals a stronger charge transfer process than the d = 3 nm sample. A combination of EXAFS and XANES data reveals that most of the Co elements form metallic Co and these phases tend to be surrounded by graphitic neighbors with quasi-sp^2 orbital configurations after RTA. Therefore, in RTA samples, the unexpected EB effect might be associated with the interfacial interaction between metallic Co and C.

High resolution transmission electron microscopy (HRTEM) measurements provide further information regarding microstructures. Figure 3 shows the HRTEM images of the d = 3 nm sample with and without RTA. For the as-grown sample (Figure 3 inset), a multilayered structure with a periodic parallel dark lines from "quasi 2D" Co layers, separated by C nominal layers, was observed. The *a*-C region show a gray ''gravel-like'' appearance that can be modeled as a random network. Some of the Co diffused outward during the sputtering process. Therefore, the average spacing between Co layers is less than 3 nm. Our EXAFS and XANES results suggest that some Co atoms mixed with C and formed Co-C bonding near C/Co interfaces. In contrast, for *a*-C/C after RTA, some of the Co diffused outward and formed Co clusters that contacted each other, as revealed in Fig. 3. In addition, another significant feature is that which lies at the C/Co layer. The C microstructure there has gained a less random configuration, which consists of small graphene multilayers. The dark ''worm-like'' lines that lie at the interface are consistent with a material that has partially crystallized[13,14]. The measured layer separation is about 0.34 nm, which is close to the spacing of the bulk graphite layers.

Magnetic coupling in C/Co composites. The existence of a considerable magnetic interaction between the Co and the C films could be revealed by XMCD applied to the Co-$L_{2,3}$ and C-K because XMCD, which is element selective, could determine the orbital and spin moments separately by using their respective XMCD sum rules[21,22]. Figure 4(a) shows normalized TEY XMCD spectra for Co-$L_{2,3}$ edges at 25 K from the d = 3 nm and d = 6 nm films after RTA, with an magnetic field of 1 T applied as they cooled from 300 K. Co XMCD around 779eV and 795 eV corresponds to the L_3 and L_2 magnetically coupled spin transitions, respectively. The absence of the

multiplet structures in the XMCD curves implies that only metallic Co contributes to the magnetic interactions in all the measured samples. To obtain further information concerning the magnetic interactions in these samples, the XMCD sum rules were applied to extract the orbital and spin moments of Co. The orbital (spin) moments of d = 3 nm and d = 6 nm samples after RTA are 0.076 and 0.032 (0.80 and 0.63), respectively. For d = 3 nm after RTA, the ratio of orbital to spin moment is remarkably close to that of pure Co films, while the value of d = 6 nm after RTA is smaller[23]. This reduction might result from the interactions between Co and C in d = 6 nm. However, as predicted by the theoretical studies on the branching ratio ($I(L_3)/[I(L_3)+I(L_2)]$; BR), one can detect the spin-orbit coupling as well as the localization of the 3d electrons by XAS[24-26]. Recent experimental studies observed the influence of hybridization and localization on the BR[27-30]. Hence, we had managed to subtract the backgrounds of the Co-$L_{2,3}$ spectra to obtain the BRs of those samples. We found that the BR of d = 6 nm (0.798) was larger than that of d = 3 nm (0.793), implying that the d = 6 nm sample had stronger hybridization between Co and C than the d = 3 nm sample had. This larger BR is close to the value of the small Co clusters[28]. The stronger hybridization could also explain the reduction of the orbital to spin ratio of d = 6 nm, as shown in the study on the FePt alloy clusters[29]. Note that the BR of d = 3 nm is also higher than the value of bulk Co and Co_2MnSi thin films, indicating that the interaction between Co and C in d = 3 nm samples is a bit weaker than that in d = 6 nm samples[27,28]. This is consistent with our XANES results regarding the Co K edge. This result provides evidence that the d = 6 nm sample after RTA has a stronger hybridization and weaker orbital moment because it has a stronger charge transfer process than the d = 3 nm sample has.

A small but vivid C-*K* XMCD signal could be observed from approximately 286 to 288 eV for d = 3 nm and d = 6 nm samples after RTA, as shown in Fig. 4(b). Spectra features in this region were expected to correspond to the C $1s \rightarrow \pi^*$ transition[31,32]. Therefore, the finite XMCD signal indicates the presence of the induced magnetic moment of C atoms, which may have originated from the strong hybridization between C π^* and transition metal 3d valence band states, as predicted by the enhancement of the BR of these samples. Note that the C XMCD signal has the opposite sign of the Co signal, indicating an antiparallel alignment between the Co and the C in the composites.

In addition to the C/Co hybridization evidenced by the reduction of orbital moments and induced C moment as mentioned above, the weaker XMCD signal for C and the stronger spin moment of the d = 3 nm sample after RTA give evidence about the origin of the Co/C EB effect as discussed below.

Theoretical modeling of EB in graphene multilayer/Co. By a combination of XAS, HRTEM, and element specific XMCD data, the unexpected EB effect can be related to

the interactions at the graphene multilayer/Co interface. The presence of an antiferromagnetic exchange coupling of the interfacial layers of TM and graphene with weakly induced magnetism caused by a magnetic proximity effect has been reported. However, the EB effect in TM/graphene has not been observed in these cases. The magnetic moments induced on our graphene multilayers in an *a*-C matrix are more localized than those on the graphene surface with ordered sp^2 hybridization. The localized C magnetic moments could pin the Co moments and result in a sizeable EB effect.

As has been mentioned, EB will happen when the system has coupling interfaces between FM and AFM materials and the critical temperature of the former is higher than that of the latter. Our experimental results clearly show the EB phenomena as the samples are treated with annealing processes. Results explicitly imply that the graphene style carbon of interfaces (GCI) enter AFM states after thermal annealing.

Based on the experimental results we construct a theoretical model to calculate the magnetization of Co nanoparticles as a function of particular magnetic couplings. The magnitude of the EB effect is dominated by spin alignments and can be clarified by the measurement of spin moments. The following theoretical model will take into account the spin moments of Co and C. The essential magnetic interaction in GCI is paramagnetic and it will be transformed to be AFM. We supposed that the magnetic transformations arise from the Co atoms introducing strong Coulomb interactions to GCI as the Co atoms approach the C atoms through thermal driving, and we supposed that the ground state of a system with strong Coulomb interactions tends to be AFM. As the Co atoms approach the GCI, a strong AFM coupling is formed between Co nanoparticles and the GCI through Kondo interactions; this causes the conduction carriers of GCI to achieve a certain degree of localization. Namely, the Co nanoparticles antiferromagnetically interact with GCI and the magnetic interactions between the localized conduction carriers of GCI are AFM as well. Note that the conduction carriers of GCI are localized but still possess a certain degrees of freedom in conduction to achieve Kondo interactions; furthermore, because the carriers are localized, their hopping integrals are less than that of graphene. Essentially, the magnetization of Co is induced from the RKKY interaction via second order Kondo interactions, where the conduction carriers of GCI are the medium.

The Hamiltonian of the model is,

$$H = H_0 + H_K + H_J, \qquad (1)$$

H_0 is the conduction band of graphited carbon. We set the structure of graphited carbon to a graphene structure. The formula of H_0 is,

$$H_0 = \sum_{k,\sigma} \epsilon_k \, c^{+}_{k,\sigma} c_{k,\sigma}. \qquad (2)$$

ϵ_k is the band dispersion of the conduction band of GCI in the momentum k

representation; σ is the spin index of the conduction carriers; their creation and annihilation operators are $c^{+}$and c, respectively. The band dispersion ϵ_k is derived from the hopping integral t and the structure dispersion factor of graphene, $\gamma_k = \left(1 + 4\cos\left(\frac{1}{2}\sqrt{k_x}\right)\cos\left(\frac{k_y}{2}\right) + 4\cos\left(\frac{k_y}{2}\right)^2\right)^{\frac{1}{2}}$, and can be written as $\epsilon_k = \pm t\,\gamma_k$.

H_K, which represents the Kondo interactions between the local magnetic moments of Co nanoparticles and the conduction carriers of GCI, is written as,

$$H_k = J_k c \sum_i S_i \cdot \sigma_i, \quad (3)$$

where J_k is the antiferromagnetic Kondo coupling between the magnetic moment of Co nanoparticles, S_i, and the spins, σ, of conduction carriers of GCI. The constant c represents the density of magnetic local moment on each carbon site, and i is the site index.

H_J, induced from the Coulomb interactions by Co nanoparticles, represents the AFM interactions between the spins of conduction carriers of GCI, and can be written as,

$$H_J = J \sum_{ij} \sigma_i \cdot \sigma_j, \quad (4)$$

where J is the antiferromagnetic coupling and σ_i represents the spin of conduction carriers in carbon site i.

To calculate the expectation value of magnetic moments of local spins of Co nanoparticles, m ($\langle S_z \rangle$), Green's function theory was employed, and the magnon dispersion could be calculated. The magnon excitation can be written in a form that encapsulates Eq.(6) and Eq.(7),

$$\omega(q) = -cJ_k\langle\sigma_z\rangle + \frac{1}{2}c^2 J_k \sum_p \frac{(6)}{(7)}. \quad (5)$$

ω(q), is the magnon dispersion as a function of magnon momentum q, which can be solved self-consistently because Eq. (7) is also a function of ω(q); where Eq.(6) and Eq.(7) in Eq.(5) are, Eq.(6) = $\langle c^{+}_{p+q,\uparrow} c_{p+q,\uparrow}\rangle - \langle c^{+}_{p,\downarrow} c_{p,\downarrow}\rangle$ and

Eq.(7) = $\omega(q) - \epsilon_{p,\downarrow} + \epsilon_{p+q,\uparrow} + 6J\langle\sigma_z\rangle - J\gamma_q \sum_{p'}(\langle c^{+}_{p'+q,\uparrow} c_{p'+q,\uparrow}\rangle - \langle c^{+}_{p',\downarrow} c_{p',\downarrow}\rangle)$; $\langle\sigma_z\rangle$ is the expectation value of magnetic moment of conduction carriers of graphited carbon; γ_q is the structure dispersion factor; the spin dependent band dispersion can be written in the form, $\epsilon_{p,\sigma} = \epsilon_p + \sigma J_k m$.

As the magnon dispersion is obtained in terms of the expectation value of the magnetic moment of Co nanoparticles, m can be calculated in terms of Callen's formula,

$$m = \frac{[S-\Phi(S)][1+\Phi(S)]^{2S+1} + [S+1+\Phi(S)][\Phi(S)]^{2S+1}}{[1+\Phi(S)]^{2S+1} - [\Phi(S)]^{2S+1}}, \quad (8)$$

$\Phi(S)$ is called the magnon number function and it can be written as $\Phi(S) =$

$\sum_q \frac{1}{\exp(\beta\omega(q))-1)}$ and β is the inverse of temperature energy, $\beta = 1/\mathrm{K_b}T$.

In our model the J is less than $\mathrm{J_k}$ because Co is a strong ferromagnetic material and the antiferromagnetic coupling J is a second order parameter. For this reason even though the conduction carriers of GCI are antiferromagnetic, when they interact, there still exists a small value of ferromagnetization $\langle\sigma_z\rangle$.

Fig 5. The expectation value of magnetic local moment *m* in Co nanoparticles at temperature 10 K. (a) The magnetic moment *m* as a function of $\mathrm{J_k}$ for $\mathrm{J} = 0.1$ and $\mathrm{J} = 0.2$, respectively. (b) The magnetic moment *m* as a function of J for $\mathrm{J_k} = 1$ and $\mathrm{J_k} = 1.5$, respectively. The unit of couplings scaled by hopping integral of conduction band is set to 1 and the *c* value in Eq.(3) is set to 0.1 as well.

Our theoretical results in Fig. 5(a) show that the Kondo interaction increases the Co magnetization, which is consistent with the experimental results as shown in Fig. 1, where the magnetization of samples at zero magnetic field increases after thermal annealing because thermal annealing enhances the Kondo interaction. An obvious transition in each curve of Fig. 5 (a) arises from a competition between both AFM interactions, namely: the Kondo interaction between Co nanoparticles and GCI, and the AFM interactions between conduction carriers of GCI. Both competing interactions will cause spin frustrations, as $\mathrm{J_k}$ increases a threshold is reached and the magnetic frustration on GCI is suppressed. Essentially, the transition happens at the same time as the suppression of the magnetic frustration. Interestingly, the increase of J will enhance the magnetization of Co, as shown in Fig. 5(b). The enhancement of magnetization with the increase of J is due to the increase of spin frustration on GCI, which tends to promote the RKKY interaction. Eventually, as this transformation proceeds, $\mathrm{J_k}$ and J are the dominant and secondary factors for forming Co magnetization. Therefore, the larger spin moments and the weaker C XMCD signals measured by XMCD of the d = 3 nm sample after RTA indicate that the d = 3 nm sample has larger $\mathrm{J_k}$ and J than those of d = 6 nm sample after RTA, resulting in a stronger EB effect that can be observed by a super-conducting quantum interference device (SQUID).

Conclusions

In conclusion, an unexpected EB effect can be observed in graphene multilayer/Co composites synthesized through RTA on Co/*a*-C multilayers. The XMCD signals of Co and C with opposite signs reveal an antiparallel alignment between the metallic Co and the sp^2-bonded C in the composites. The disordered nature of *a*-C causes a localized spin moment that can pin the Co spin moment and is responsible for the pronounced EB effect. The present study provides a deeper understanding of EB in Co/C, which may be important for guiding the design and fabrication of C based spintronics devices.

Methods

Discontinuous $[C(d)/Co(3\ nm)]_5/C(3\ nm)$ multilayers with $d = 3$ nm and $d = 6$ nm were fabricated on a quartz substrate at ambient temperature using a radio frequency sputtering system with a base pressure of $1x10^{-6}$ Torr. Several Co/C multilayers were deposited using sputtering with Ar gas at a process pressure of $2x10^{-2}$ Torr alternately on C and Co targets for five cycles. The Co/C multilayers were deposited alternately on C and Co targets for five cycles. After deposition, RTA was performed at 600°C for 2 min in a vacuum chamber that was evacuated to 1×10^{-6} Torr. Magnetization measurements were made using a SQUID (MPMS, Quantum Design Co., Ltd.). The field cooling hysteresis loops were measured at 10 K under cooling fields of 1T. XAS measurements were made in the wiggler-C beam line 17 (at the Taiwan Light Source in Hsinchu, Taiwan) and a fluorescent yield spectrum was obtained to determine the bulk properties of the films. XMCD measurements were performed at the Dragon beam line BL11A of Taiwan Light Source. XMCD spectra were measured by the total electron yield method and the circular polarization of the incident photons was fixed and the direction of the applied magnetic field was changed. HRTEM measurements were performed on a JEOL-JEM2100F instrument operating at an acceleration voltage of 200 kV.

Reference

1. Nogués, J. & Schuller, I. K. Exchange bias. *J. Magn. Magn. Mater.* **192**, 203-232 (1999).

2. Berkowitz, A. E. & Takano, K. Exchange anisotropy-a review. *J. Magn. Magn. Mater.* **200**, 552-570 (1999).

3. Radu, F. & Zabel, H. Exchange bias effect of ferro-/antiferromagnetic heterostructures. *Springer Tr. Mod. Phys.* **227**, 97-184 (2008).

4. Binasch, C., Grünberg, P., Saurenbach, F. & Zinn, W. Enhanced magnetoresistance in layered magnetic structures with antiferromagnetic interlayer exchange. *Phys. Rev. B* **39**, 4828–4830 (1989).

5. Radu, F., Abrudan, R., Radu, I., Schmitz, D. & Zabel, H. Perpendicular exchange bias in ferromagnetic spin valves. *Nat. Commun*. **3** 715 (2012).

6. Dedkov, Yu. S. & Fonin, M. Electronic and magnetic properties of the graphene–ferromagnet interface. *New J. Phys.* **12**, 125004 (2010).

7. Liu, W. Q. *et al.* Atomic-Scale Interfacial Magnetism in Fe/Graphene Heterojunction. *Sci. rep.* **5**, 11911 (2015).

8. Moorsom, T. *et al.* Spin-polarized electron transfer in ferromagnet/C_{60} interfaces. *Phys. Rev. B* **90**, 125311 (2014).

9. Hsu, H. S., Chien, P. C., Sun, S. J., Chang, Y. Y. & Lee, C. H. Room temperature ferromagnetism in Co-doped amorphous carbon composites from the spin polarized semiconductor band. *Appl. Phys. Lett.* **105**, 042410 (2014).

10. Hsu, H. S. *et al.* Tunable interface magnetic-optical properties of Co doped amorphous carbon film induced by charge transfer after acid treatment. *Carbon* **77**, 398 (2014).

11. Manna, P. K. & Yusuf, S. M. Two interface effect: Exchange bias and magnetic proximity. *Physics Reports* **535**, 61-99 (2014).

12. Robertson, J. Diamond like amorphous carbon. *Mater. Sci. Eng.* **R37**, 129-281 (2002).

13. Hayashi, T., Hirono, S., Tomita, M. & Umemura, S. Magnetic thin film of cobalt nanocrystals encapsulated in graphite-like carbon. *Nature* **381**, 772-774 (1996).

14. Ramírez, A. G., Itoh, T. & Sinclair, R. Crystallization oh amorphous carbon thin film in the presence of magnetic media. *J. Appl. Phys.* **85**, 1508 (1999).

15. Host, J. J. *et al.* Effect of annealing on the structure and magnetic properties of graphite encapsulated nickel and cobalt nanocrystals. *J. Appl. Phys.* **83**, 793 (1998).

16. Zheng, M. *et al.* Metal-catalyzed crystallization of amorphous carbon to graphene. *Appl. Phys. Lett.* **96**, 063110 (2010).

17. Lu, A. H. *et al*. Highly stable carbon-protected cobalt nanoparticles and graphite shells. *Chem. Commun.* 98-100 (2005).

18. Su, H. C. *et al.* Connection between orbital moment enhancement and exchange bias in a $[Ni_{80}Fe_{20}/Mn]_3$ multilayer. *Phys. Rev. B* **87**, 014402 (2013).

19. Hsu, H. S. *et al.* Sizeable magnetic circular dichroism of artificially precipitated Co clusters in amorphous carbon. *AIP adv.* **2**, 032142 (2012).

20. Kolobov, A. V., Tominaga, J., Zvonareva, T. K., Ivanov Omskii, V. I., & Oyanagi, H. Local structure of Co nanocrystals embedded in hydrogenated amorphous carbon: An x-ray absorption study. *J. Appl. Phys.* **92**, 6195 (2002).

21. Thole, B. T., Carra, P., Sette, F. & van der Laan, G. X-ray circular dichroism as a probe of orbital magnetization. *Phys. Rev. Lett.* **68**, 1943-1946 (1992).

22. Carra, P., Thole, B. T., Altarelli, M. & Wang, X. X-ray circular dichroism and local magnetic fields. *Phys. Rev. Lett.* **70**, 694-697 (1993).

23. Chen, C. T. *et al.* Experimental confirmation of the XMCD sum rules for iron and cobalt. *Phys. Rev. Lett.* **75**, 152-155 (1995).

24. Thole, B. T. & van der Laan, G. Branching ratio in x-ray absorption spectroscopy. *Phys. Rev. B* **38**, 3158 (1988).

25. Thole, B. T. & van der Laan, G. Linear relation between x-ray absorption branching ratio and valence-band spin-orbit expectation value. *Phys. Rev. B* **38**, 1943 (1988).

26. Van der Laan, G. & Thole, B. T. Local probe for spin-orbit interaction. *Phys. Rev. Lett.* **60**, 1977 (1988).

27. Telling, N. D. *et al.* Temperature dependence of the interface moments in Co_2MnSi thin films. *Appl. Phys. Lett.* **92**, 192503 (2008).

28. Lau, J. T. *et al.* Size dependence of $L_{2,3}$ branching ratio and 2p core-hole screening in X-ray absorption of metal clusters. *Phys. Rev. Lett.* **101**, 153401 (2008)

29. Chen, K. *et al.* Hybridization and magnetism in small FePt alloy clusters. *New. J. Phys.* **14**, 123005 (2012)

30. Akgul, G., Akgul, F. A. & Ufuktepe, Y. Investigation of thickness dependence on electronic structures of iron and nickel thin films by L-edge X-ray absorption spectroscopy. *Vacuum* **99**, 211 (2014).

31. Jaouen, N. *et al.* Spin and orbital magnetic moments in carbon-encapsulated $Fe_{50}Pt_{50}$ nanoparticles. *Phys. Rev. B* **76**, 104421 (2007).

32. Muramatsu, Y., Shimomura, K., Katayama, T. & Gullikson, E. M. Total electron yield soft X-ray absorption spectroscopy in the C *K* region of the mixtures of graphitic carbons and diamond for quantitative analysis of the sp^2/sp^3-hybridized carbon ratio. *Jpn. J. Appl. Phys.* **48**, 066514 (2009)

Figure captions

Fig. 1 The M-H data for (a) d=3nm and (b) d=6nm Co:*a*-C composites without and with RTA at 10 K and 300 K. (c) The $T^{1/2}$ dependence of Hc(T) of d=3nm and d=6nm samples after RTA, with the dash line being a guide to the eye. (d) Temperature dependence of the exchange bias field, H_E, of the d=3nm and d=6nm samples after RTA.

Fig. 2 (a) The FT amplitude of EXAFS of d=3nm and d=6nm Co:*a*-C composites without and with RTA as well as metallic Co foil. (b) XANES for these samples at Co *K*-edge. Metallic Co foil data is provided for reference.

Fig. 3 The HRTEM image of the d=3nm Co:*a*-C composites with RTA. The graphene multilayers region showing a characteristic 0.34nm interlaminar spacing. The inset shows the HRTEM image without RTA for underscoring how essential the annealing is in the metal-contact-induced graphitization mechanism.

Fig. 4 XMCD spectra of the d=3nm and d=6nm Co:*a*-C composites with RTA: absorption spectra measured for two opposite orientations of the magnetization are shown in the upper part for the Co $L_{2,3}$- (a) and C *K*-edges (b). The corresponding diff erences are shown in the lower part of the respective figures.

Fig. 5 The expectation value of magnetic local moment m in Co nanopartilces at temperature 10 K. (a)The magnetic moment m as a function of J_k for J=0.1 and J=0.2, respectively. (b) The magnetic moment m as a function of J for J_k=1 and J_k=1.5, respectively. The unit of couplings scaled by hopping integral of conduction band is set to 1 and the c value in eq.(3) is set to 0.1 as well.

Fig. 1

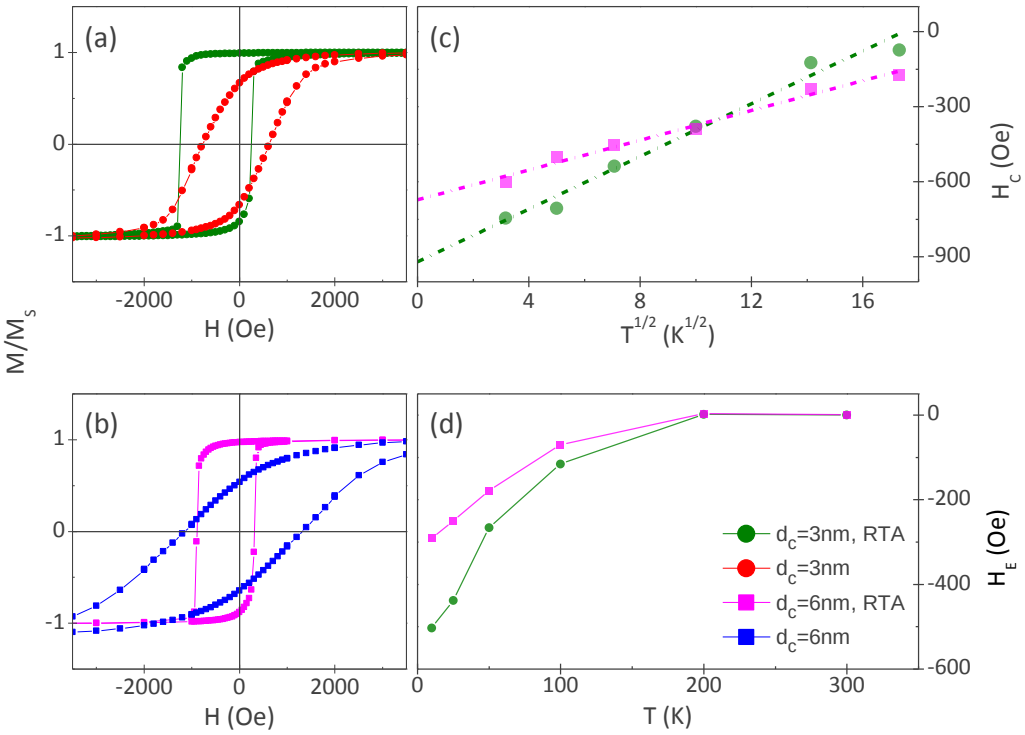
(a)
(b)
(c)
(d)
M/M_S
H (Oe)
T^1/2 (K^1/2)
H_C (Oe)
T (K)
H_E (Oe)
d_C=3nm, RTA
d_C=3nm
d_C=6nm, RTA
d_C=6nm

Fig. 2

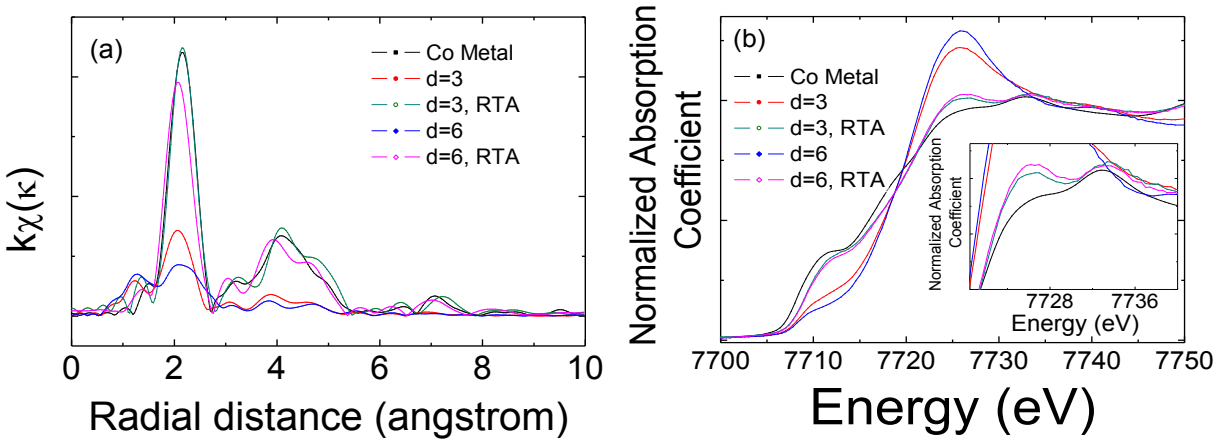
(a)
Co Metal
d=3
d=3, RTA
d=6
d=6, RTA
kχ(κ)
0
2
4
6
8
10
Radial distance (angstrom)
(b)
Co Metal
d=3
d=3, RTA
d=6
d=6, RTA
Normalized Absorption Coefficient
7700
7710
7720
7730
7740
7750
Energy (eV)
Normalized Absorption Coefficient
7728
7736
Energy (eV)

Fig. 3

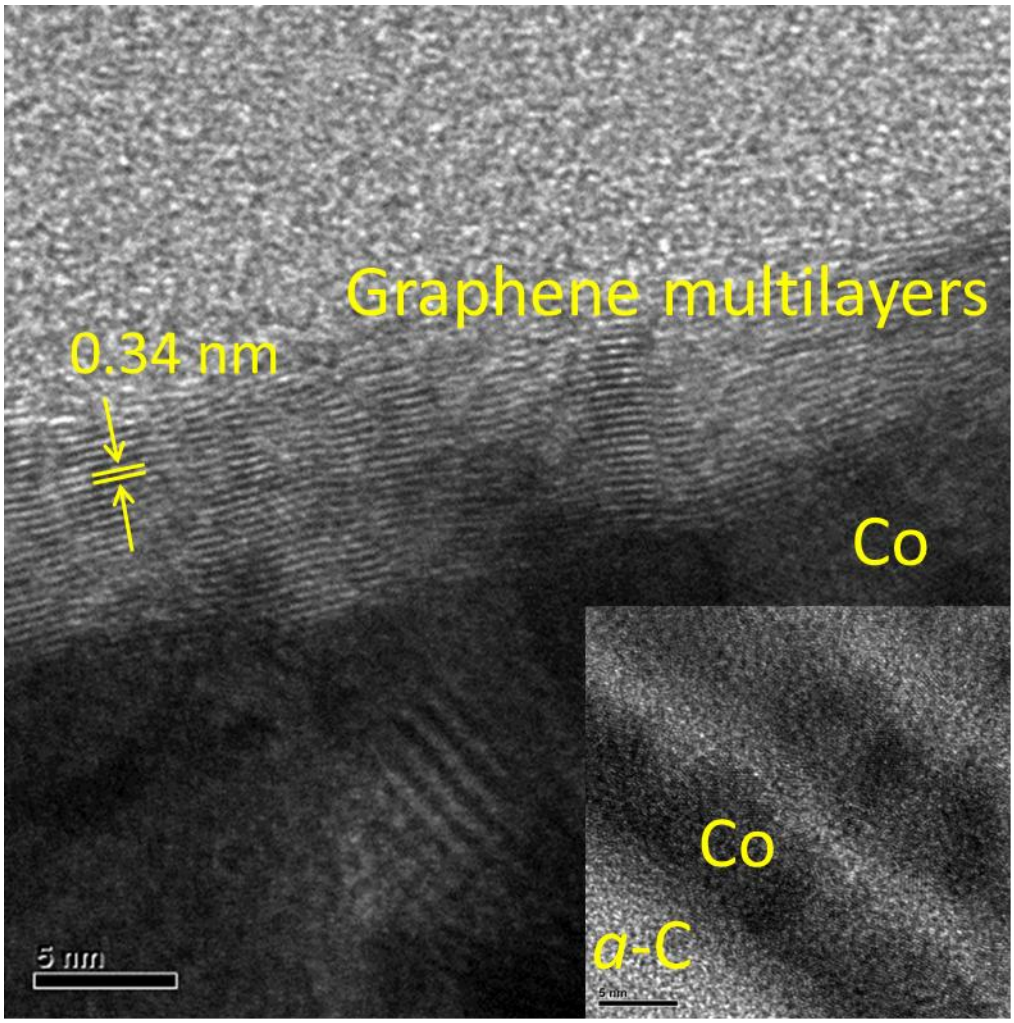

Fig. 4

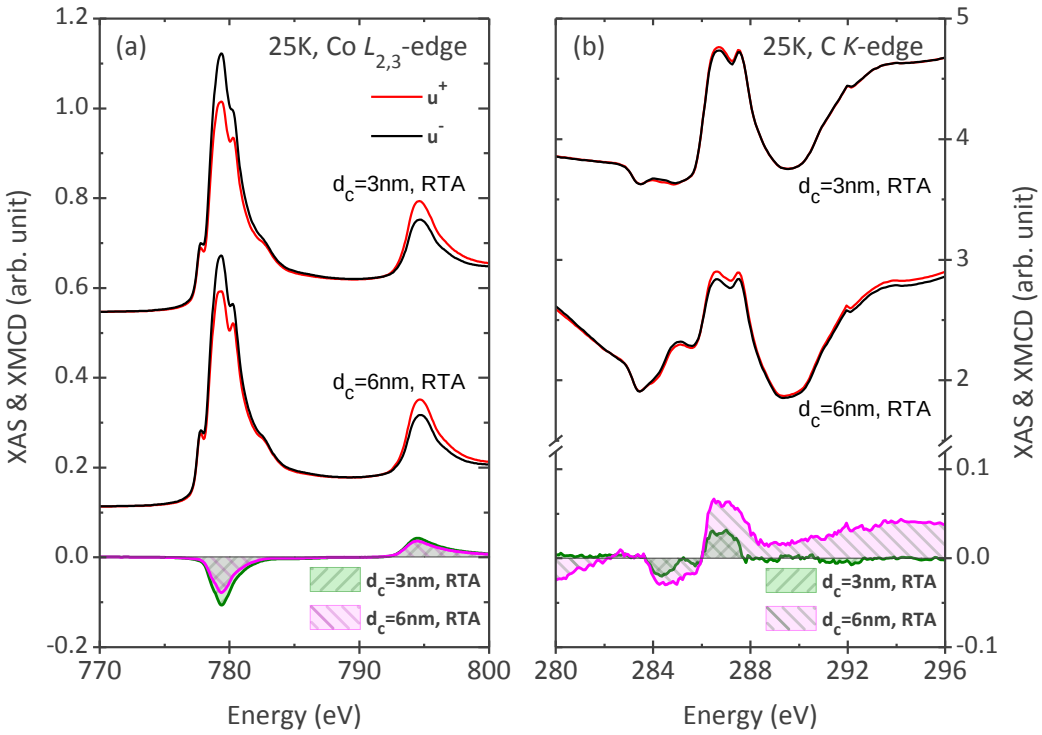
(a)
25K, Co $L_{2,3}$-edge
u^+
u^-
d_c=3nm, RTA
d_c=6nm, RTA
d_c=3nm, RTA
d_c=6nm, RTA
XAS & XMCD (arb. unit)
Energy (eV)
(b)
25K, C K-edge
d_c=3nm, RTA
d_c=6nm, RTA
d_c=3nm, RTA
d_c=6nm, RTA
XAS & XMCD (arb. unit)
Energy (eV)

Fig. 5

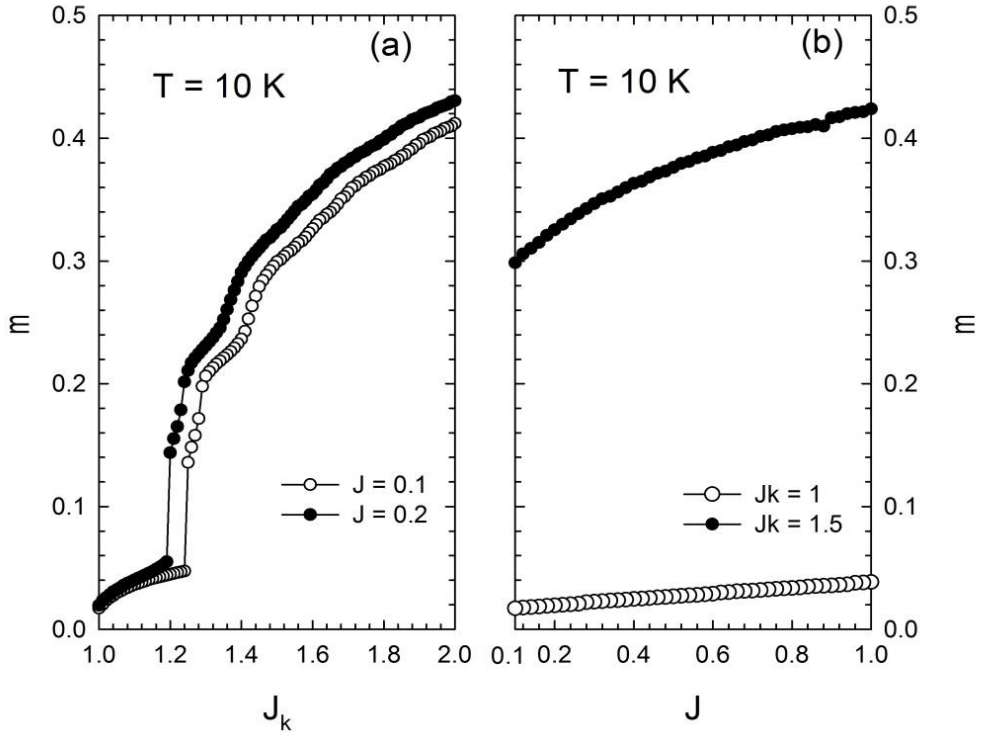

Acknowledgements

The authors would like to thank the National Science Council of the Republic of China, Taiwan, for financially supporting this research under Contract No. MOST 104-2112-M-153 -002 -MY3. 請各位夥伴看是否欲加上您致謝的計畫編號

Author contributions

H.S.H. conceived and designed the experiments. Y.Y.C. synthesized and characterized the composites and performed the experiments. Y.Y.C., H.J.L., and C.T.C performed XAS/XMCD experiments and analysis. S.J.S contributed towards theoretical calculations. S.Z conducted HRTEM analysis. C.R.L. and S.G.O participated in the discussion of magnetic results. H.S.H., Y.Y.C. and S.J.S. analyzed the data and wrote the manuscript. All authors discussed the results and commented on the manuscript.